

# Geometry of the vapor layer under a Leidenfrost hydrogel sphere

Vicente L. Diaz-Melian,<sup>1,\*</sup> Isaac C. D. Lenton,<sup>1</sup> Jack Binysh,<sup>2</sup> Anton Souslov,<sup>3</sup> and Scott R. Waitukaitis<sup>1</sup>

<sup>1</sup>*Institute of Science and Technology Austria, Am Campus 1, 3400 Klosterneuburg, Austria*

<sup>2</sup>*Institute of Physics, Univ. Amsterdam, Science Park 904, 1098 XH Amsterdam, The Netherlands*

<sup>3</sup>*TCM Group, Cavendish Laboratory, JJ Thomson Avenue, Cambridge, CB3 0HE UK*

(Dated: July 8, 2025)

A floating Leidenfrost droplet exhibits curvature inversion of its underside, due to the balance of vapor pressure and surface tension. Using interferometric imaging, we find different behavior for a levitated hydrogel sphere. Curvature inversion is observed briefly just after deposition, but quickly gives way to a steady state with no inversion. We show the essential role of vaporization on shaping the underbelly of the hydrogel, adding a new component to the interplay between vapor pressure and elastic forces.

A liquid droplet deposited on a hot surface just above its boiling point evaporates quickly and violently. However, at much higher temperatures, an unexpected phenomenon occurs: the droplet levitates and remains floating above the surface for extended periods. This counterintuitive behavior is known as the Leidenfrost effect, and it arises due to the formation of a vapor layer beneath the droplet. This vapor layer insulates the droplet from the surface and simultaneously supports its weight, allowing it to levitate [1–3]. The Leidenfrost effect serves as a fundamental framework for understanding fluid–structure interactions, with industrial applications ranging from controllable wetting [4–6] to optimized heat exchange [7–9]. Leidenfrost physics has been extensively studied in simple liquids [10–17] and sublimable solids [18–21], where both experimental [22–29] and theoretical [30–33] efforts have characterized droplet morphology and surface temperature profiles in relation to the droplet’s ability to float. More recently, this phenomenon has been extended to vaporizable soft solids, such as hydrogel spheres, which exhibit two distinct types of Leidenfrost behavior [34, 35]. At high approach velocities, these spheres make contact with the surface, leading to high-frequency surface oscillations that harvest energy and produce bouncing behavior [34]. At low velocities, they enter a ‘normal’ floating state that, in many respects, resembles the classical liquid Leidenfrost state [35].

The morphology beneath Leidenfrost droplets arises from a competition between surface tension and vapor pressure. Burton *et al.* investigated this balance experimentally using high-speed interferometric imaging through a transparent, heated substrate [22]. Their results revealed a rim with saddle points and extrema, indicating that the lower facet of the droplet is not flat but exhibits a curvature inversion—i.e., a ‘pocket’ of vapor is trapped below the drop. This shape had been predicted by Snoeijer *et al.*, whose analytical work showed that the curvature inversion becomes more pronounced with increasing droplet radius [30]. For soft vaporizable solids, the shape of the underbelly should reflect a bal-

ance between elastic forces and vapor pressure. However, unlike simple fluids, soft solids, gels, and emulsions exhibit a complex interplay between short-term viscoelastic response and long-term irreversible shape changes [36], resulting in an inherently multiscale behavior [37].

In this work, we experimentally measure the geometry underneath a Leidenfrost-floating soft solid. We find that the curvature inversion predicted for elastic objects [38] is lost over time due to vaporization-induced shape changes. An initial elastic inversion forms as the hydrogel sphere approaches the hot surface but rapidly transitions to a steady state without a vapor pocket and with stable upward curvature. We propose that this transition results from irreversible deformation of the sphere caused by continued vaporization. Using simulations, we qualitatively reproduce our observations, highlighting the crucial contribution of heat flux in driving the vaporization process. Our results reveal a fundamental coupling between vaporization and shape change in Leidenfrost solids—a coupling absent in their liquid counterparts.

The experimental setup is shown in Fig. 1(a). We use a suction cup to attach a hydrogel sphere (radius  $a \approx 7$  mm) to a string, which is connected to a weight sensor and piezo motor. The hot surface below the hydrogel is a wedged sapphire window, chosen for its good heat conduction and transparency. We lower the hydrogel toward the substrate at a constant speed ( $\sim 33$   $\mu\text{m/s}$ ) with the piezo motor (Agilis AG-LS25). The window sits on a hot plate, with an aperture that permits an expanded, 633 nm laser (Thorlabs HNL210L) to pass through. This beam reflects off the upper surface of the window and the lower surface of the hydrogel to create an interference pattern, which is recorded by a camera (Phantom v1612). A second camera (Basler a2A 1920) simultaneously records from the side.

Figure 1(b) first shows the steady-state interference pattern of a liquid droplet. A prominent rim of saddle and extrema points indicates the well-known curvature inversion [22], which results from the balance between surface tension and vapor pressure. In the case of a soft solid, one naturally suspects that the interplay of elasticity and vapor pressure should create a similar inversion, as our recent model has indicated [38]. Our experiments, however, reveal that such reasoning prevails only briefly.

\* vicenteluis.diazmelian@ista.ac.at

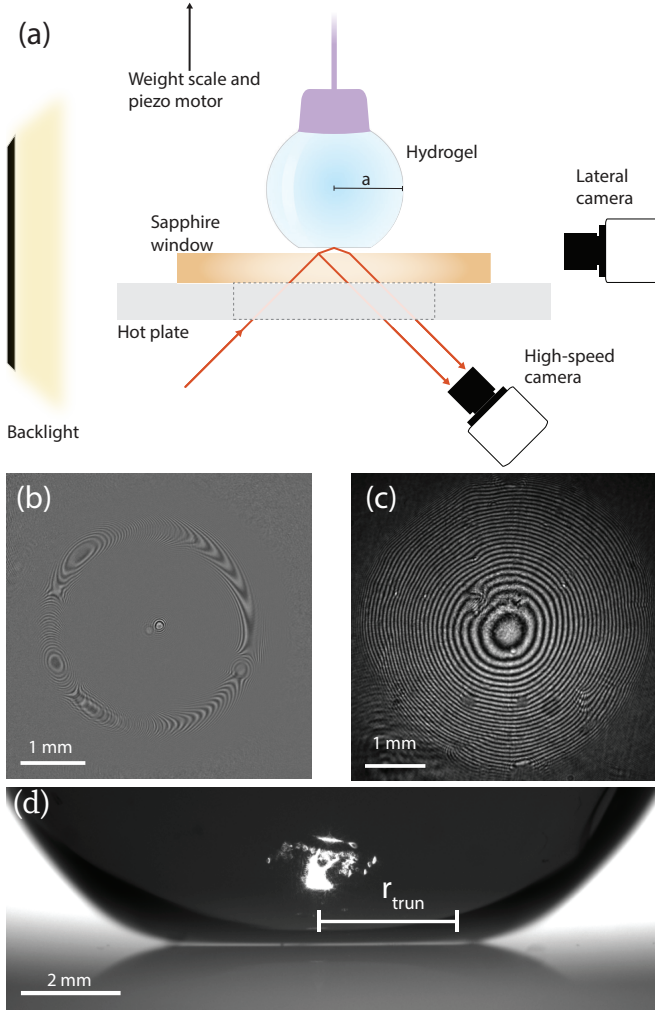


FIG. 1. Experimental setup and key observations. (a) We use a piezo motor to slowly lower a hydrogel sphere connected to a string toward a hot ( $\sim 220^\circ\text{C}$ ) sapphire window. A weight sensor at the top of the string allows us to determine how much of the hydrogel is supported by the vapor layer. The hot plate below the sapphire window has an aperture that allows an expanded, 633 nm laser to pass through. A high-speed camera records the interference pattern produced from reflections at the top of the window and the bottom of the hydrogel, while a second camera records from the side. (b) When a water droplet is placed on the window, we observe a steady state with a rim pattern and both saddle/minima features, indicating a curvature inversion beneath the droplet. (c) In contrast, the steady-state pattern for a hydrogel only has concentric rings, indicating the absence of curvature inversion. (d) View of the gap below the hydrogel as seen by the side-view camera, with truncated radius ( $r_{\text{trun}}$ ) indicated.

As shown in Fig. 1(c), the steady state for a floating hydrogel has no rim of saddles/minima, but rather just interference pattern of concentric rings, which indicate the absence of curvature inversion. By comparing the radius at which the rings are no longer visible to the ‘floating’ radius,  $r_{\text{trun}}$ , of the hydrogel seen from the side-view

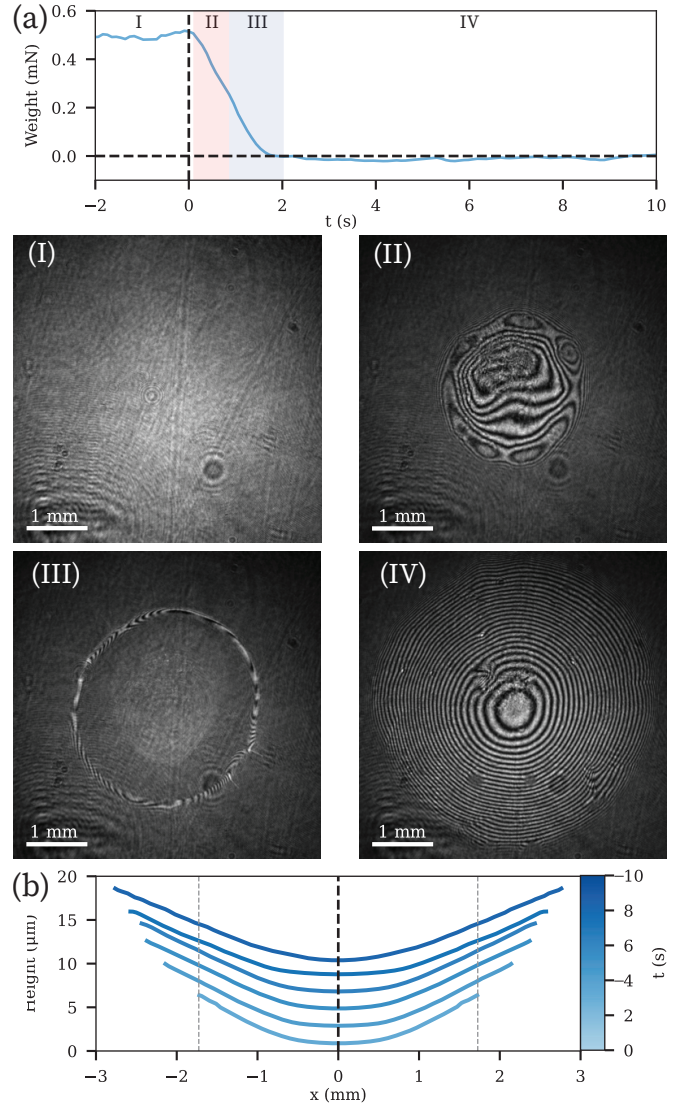


FIG. 2. Time evolution of the interference pattern. (a) Weight of the hydrogel supported by the vapor as a function of time, with key points indicated (I-IV) and corresponding interferometric images. At region I, the weight is carried fully by the string, and no features are present in the interference pattern. At  $t = 0$ , the hydrogel starts interacting with the vapor, and until region II the interference pattern shows a distinct rim with saddle/minima points, indicating curvature inversion (red box). In the following region III (blue box), the rim destabilizes and the underside of the hydrogel enters into oscillations. On region IV, the oscillations disappear, resulting in equilibrium floating of the hydrogel and a stable interference pattern without any curvature inversion. (b) Reconstructed height profile of the hydrogel underside in region IV at different times

camera (Fig. 1(d)), we conclude that the absence of an inversion rim is not due to any limit in the field of view of our interferometric images (see Supplemental Material 1).

In Fig. 2, we present the time evolution towards this steady state in detail. Panel (a) shows the weight of

the hydrogel, supported by the vapor layer as a function of time, with key regimes indicated by Roman numerals (I-IV) and colors. In regime I, the weight is fully supported by the string, indicating that no vapor layer has formed; hence no interference features are present (Fig. 2(a) image I). At  $t = 0$ , the hydrogel just begins interacting with the vapor, and in the red region (II) we observe a curvature-inversion rim (image II). We only observe this inversion very briefly—in the subsequent blue region (III) the rim destabilizes, giving way to rapid (kHz) oscillations that are accompanied by audible whistling. These oscillations are also short lived; after the weight is fully supported by the vapor, the stable regime (IV) is reached, where only concentric rings are present and there is no inversion. In this regime, the floating radius grows steadily with time, and the number of rings steadily increases (Supplemental Video 1). Fig. 2(b) shows the reconstructed height profiles in the region IV at different times, as determined by extracting the radial extent of each ring and assigning a height difference of one half wavelength. Due to the fact that absent inversion downward curvature is not possible, we conclude that the stable curvature is upward, *i.e.* within the floating radius the hydrogel is closest to the surface in the center and farthest away at the edges.

Why does the curvature inversion disappear? And what causes the upward curvature in the steady state? When the hydrogel first approaches the surface, its undeformed shape is perfectly spherical, and its initial interaction with the vapor leads to the brief appearance of the anticipated elastic curvature inversion [38]. This is unstable, resulting in the oscillations observed in regime III of Fig. 2. We can explain the subsequent upward curvature through interactions with the hot surface, which cause not only reversible elastic shape changes but also irreversible changes due to vaporization. As soon as the sphere starts vaporizing, it is no longer a sphere, as every parcel of vapor lost permanently alters the shape. Moreover, as elastic forces and vapor pressure conspire to create the initial curvature inversion and oscillations, the edge of the floating region is on average closer to the surface than the center, hence it vaporizes faster and disappears. The second key idea is that vaporization is faster at the edge than the center. Two candidate mechanisms might cause this: (1) the hydrogel cools the substrate locally, resulting in a temperature profile that is colder at the center and hotter at the edges, or (2) the vaporization rate depends on the local vapor concentration, which is higher at the center and lower at the edges. Either or both of these differential vaporization mechanisms would lead to a net upward curvature in the steady-state shape. Although elastic deformations must also occur throughout, the dominant contribution to the final shape arises from irreversible mass loss due to vaporization. Thus, even after the initial curvature inversion disappears, the system does not revert to a flat or inverted profile, but instead continued enhanced evaporation near the edge sculpts the hydrogel into a state with upward curvature.

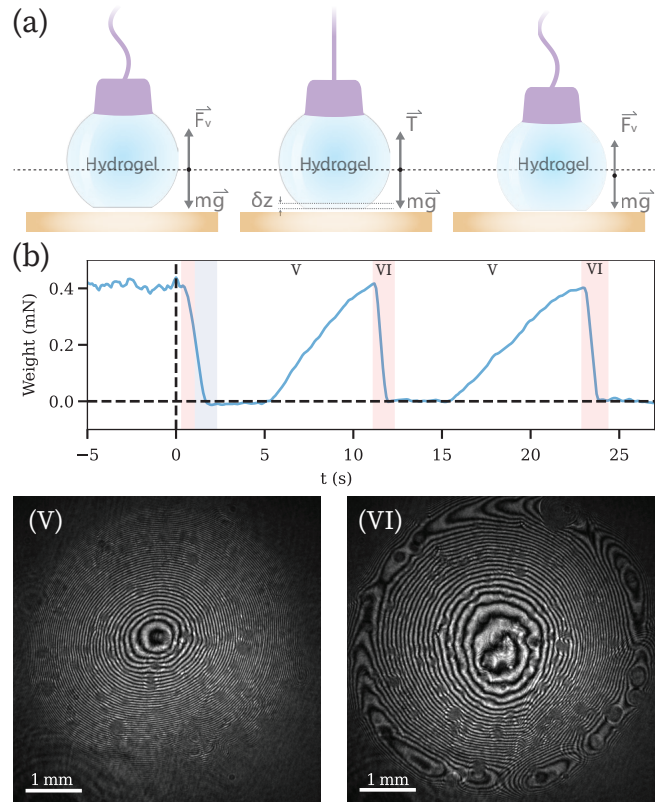


FIG. 3. Temporary recovery of curvature inversion via elastic reloading. (a) To re-load the hydrogel elastically, and hence temporarily recover curvature inversion, we start by lowering it just beyond the point where all weight is carried by the vapor, leaving the string slightly loose (left). We then let vaporization occur until a small amount of hydrogel,  $\delta z$ , is removed, resulting in the string again becoming taught (middle). Upon lowering the hydrogel again, the vapor elastically deforms the hydrogel to recover curvature inversion, but only temporarily as vaporization quickly acts to take it away (right). (b) Weight *vs.* time during multiple iterations of the elastic reloading process. Region V corresponds to the recovery of the weight by the string (middle panel a). Region VI, within the red box, highlights the elastic interplay between the hydrogel and the vapor layer. Once again, evaporation overcomes the curvature inversion and the hydrogel reaches a stable floating regime without curvature inversion.

We lend evidence to these ideas with the experiment sketched in Fig. 3(a). We take a new hydrogel and begin by lowering it toward the hot surface. As soon as its weight is fully carried by the vapor, we stop the piezo motor, which leaves a slight slack in the string. Now we let the sphere float, causing a small vertical slab of thickness  $\delta z$  to be removed due to vaporization. When this exceeds the slack, the string starts carrying the weight, the gap becomes larger, and the vaporization rate is reduced. This leads to an elastic unloading of the sphere and a decoupling from the vaporization-dominant mechanism. When the weight has been fully recovered by the string, we lower the sphere again to re-load it elas-



tically and re-initiate the vaporization mechanism, with the prediction that we should (fleetingly) recover the curvature inversion. As shown in Fig. 3(b), this prediction bears true. The upper plot shows the weight carried by the vapor throughout the process, where the interference between the vapor/string for multiple iterations is clearly visible. The images below show the repeatable recovery of the curvature inversion. In V, *i.e.*, after the initial inversion is lost and the sphere has been floating, there is only upward curvature. However, in VI, just after we have elastically reloaded the sphere, the inversion ring reappears—only to quickly disappear again once because vaporization. (For the full evolution, see Supplemental Video 2.) This highlights the essential role of vaporization-induced shape changes in the physics at hand, and in particular how they quickly override elasticity.

Of the two differential vaporization mechanisms proposed, which is more important? As we motivate in the Supplementary material, the effect of the concentration-driven mechanism can be expected to be smaller than the effect of the substrate temperature-gradient mechanism. Therefore, we focus on the hydrogel’s non-uniform cooling of the substrate to further support vaporization as the primary sculptor of the upward curvature observed underneath the hydrogel. The idea is motivated by Refs. [12], who showed that even a millimetric liquid droplet can significantly cool the substrate beneath it. The hydrogel cools the substrate, leading to a spatially and temporarily dependent temperature profile,  $T(r, t)$ . The local vaporization rate is coupled to  $T(r, t)$ , which is furthermore coupled to the local gap height  $h(r, t)$  through the balance of pressure in the lubrication layer. Though it is subdominant, the elastic response of the hydrogel likely can’t be completely ignored, and will change dramatically over time as the hydrogel’s shape is irreversibly changed.

We motivate the applicability of the proposed mechanism using a simplified situation in simulations. Our computational approach involves three steps: (1) using finite element method (FEM) simulations to calculate the radially-dependent temperature profile of the substrate underneath the hydrogel with average gap height  $h_0(t)$  and floating radius  $r_{trun}(t)$ , (2) using this temperature profile to numerically calculate the changes in the height profile (and consequently, floating radius) considering the local temperature gradient and a small time interval,  $\delta t$ , and (3) use the known force-balance equation to update the average gap height,  $h_0$ , based on the floating radius. Details on step 1, *i.e.* the FEM simulations, can be found in the Supplemental Material 1. Step two is achieved using the mass-loss equation,

$$\delta h(r) = -\frac{\kappa}{\rho L} \frac{T(r) - T_H}{h(r)} \delta t, \quad (1)$$

where  $\kappa$  is the thermal conductivity of the vapor,  $\rho$  and  $L$  are respectively the density and latent heat of the hydrogel,  $T(r)$  is the temperature at radius  $r$  of the substrate

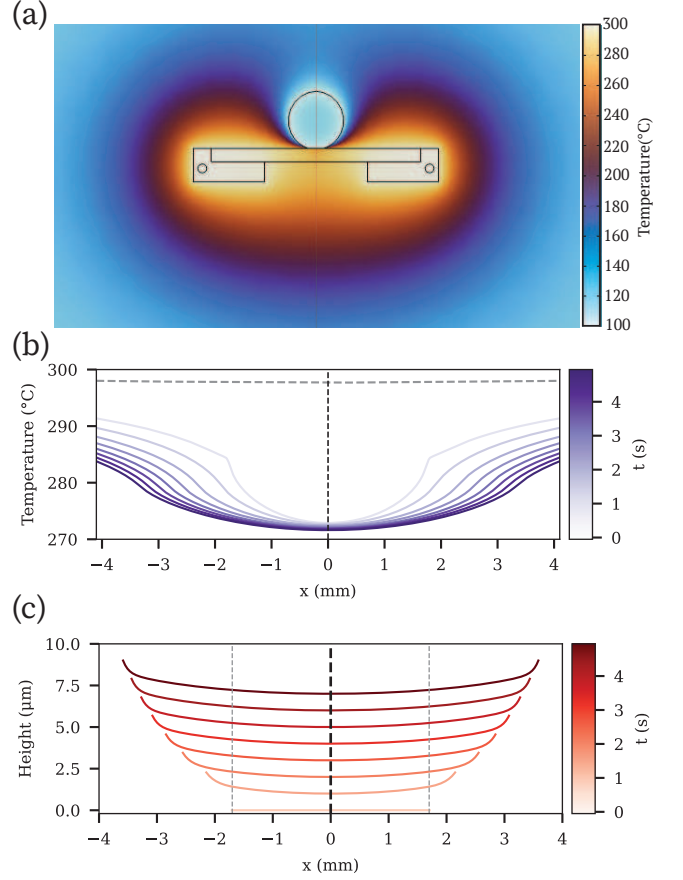


FIG. 4. Simple vaporization model. (a) We perform FEM simulations to calculate the system temperature at different truncation radii of the sphere,  $r$ , with corresponding gap heights given by Eq. 2. The sphere underside is assumed flat, justified by the fact that the variations in height profile are much smaller than the gap. (b) Temperature profile on top of the sapphire window for different times, assuming initially  $r(t_0) = r_H$ . (c) Height profile underneath the sphere *vs.* time, as calculated numerically by iteratively applying Eq. 1 to determine the changes in the height/radius profile, Eq. 2 to determine the new gap height, and then using the FEM simulations to determine the new temperature profile. See Supplemental Materials for full simulation details.

below, and  $T_H = 100^\circ \text{C}$  is the temperature of the hydrogel. Step three is achieved using the force balance equation for the integrated lubrication pressure *vis-à-vis* the weight of the sphere, given by

$$h_0(t) = \left( \frac{3\pi\eta\kappa\Delta T}{2\rho L} \right)^{\frac{1}{4}} \frac{r_{trun}(t)}{(mg)^{1/4}}. \quad (2)$$

Here,  $\eta$  is the viscosity of the vapor,  $\Delta T$  is the (average) temperature difference between the hydrogel and substrate, and  $mg$  is the weight of the hydrogel. Though this equation was originally derived for the case of liquid droplets, it was recently shown to be in good agreement for floating hydrogels [35].

Results are shown in Fig. 4, and corresponding Supple-

mental video 3. Panel a shows the calculated temperature profile in our system at the initial conditions, where we take  $r_{\text{trun}}$  to be equal to the gravity-loaded Hertzian contact radius and the gap height is calculated using this value in Eq. 2. Fig. 4(b), we show the changes to  $T(r)$  as a function of time after this initial condition. Two observations merit comment. First, the temperature in the substrate directly below the center of the hydrogel is on the order of 10% lower than at the edges. Second, due to the fact that the floating radius becomes larger as time progresses, the ‘temperature footprint’ of the hydrogel also grows with time. Finally, Fig. 4(c) shows the (relative) height profiles for different times. Like the experiments, the model produces a height profile with an upward curvature, indicating that changes in the vaporization rate due to the surface temperature profile below the sphere are a significant contributing factor for the observed phenomena.

Our results underscore the dominant role of mass loss due to vaporization in shaping the long-term height profile beneath a Leidenfrost-floating elastic solid. Although curvature inversion emerges in the early stages of a hydrogel sphere’s interaction with a hot surface—and can be briefly re-initiated via elastic reloading—it rapidly disappears as irreversible, vaporization-induced deformations proceed. Simulations show that cooling from the hydrogel generates significant differences in the temperature profile beneath the floating sphere. By assuming these

differences cause localized variations in the mass loss rate, we successfully reproduce the key features of the observed height profile evolution. While our study emphasizes vaporization-driven shape changes, the remnant influence of elasticity remains incompletely explored. A complete analytical treatment of the system—including squeeze flow in the vapor layer, elastic deformations, vaporization dynamics, substrate cooling, and the resulting force balances—is highly complex and beyond what we can assess here. These coupled processes may be more effectively studied using multi-physics simulations in future work. Future investigations are planned to quantify these effects more precisely.

This research was supported by the Scientific Service Units of The Institute of Science and Technology Austria (ISTA) through resources provided by the Miba Machine Shop, and the Scientific Computing Facility. J.B. acknowledges funding from the European Union’s Horizon research and innovation programme under the Marie Skłodowska-Curie Grant Agreement No. 101106500.

#### **CRedit Author Statement**

**VD:** Methodology, Software, Formal analysis, Investigation, Writing – Original Draft, Visualization.

**IL:** Methodology, Software, Formal analysis, Writing – Review & Editing.

**JB:** Conceptualization, Writing – Review & Editing.

**AS:** Conceptualization, Writing – Review & Editing.

**SW:** Conceptualization, Writing – Review & Editing, Supervision, Funding acquisition.

- 
- [1] A.-L. Biance, C. Clanet, and D. Quéré, *Physics of Fluids* **15**, 1632 (2003).
  - [2] D. Quéré, *Annu. Rev. Fluid Mech.* **45**, 197 (2013).
  - [3] G. Dupeux, M. Le Merrer, C. Clanet, and D. Quéré, *Phys. Rev. Lett.* **107**, 114503 (2011), publisher: American Physical Society.
  - [4] Y. Wakata, N. Zhu, X. Chen, S. Lyu, D. Lohse, X. Chao, and C. Sun, *Phys. Rev. Fluids* **8**, L061601 (2023), publisher: American Physical Society.
  - [5] M. Jiang, Y. Wang, F. Liu, H. Du, Y. Li, H. Zhang, S. To, S. Wang, C. Pan, J. Yu, D. Quéré, and Z. Wang, *Nature* **601**, 568 (2022).
  - [6] M. Shirota, M. A. van Limbeek, C. Sun, A. Prosperetti, and D. Lohse, *Phys. Rev. Lett.* **116**, 064501 (2016), publisher: American Physical Society.
  - [7] G. G. Wells, R. Ledesma-Aguilar, G. McHale, and K. Sefiane, *Nat Commun* **6**, 6390 (2015), publisher: Nature Publishing Group.
  - [8] T. Tran, H. J. J. Staat, A. Prosperetti, C. Sun, and D. Lohse, *Phys. Rev. Lett.* **108**, 036101 (2012), publisher: American Physical Society.
  - [9] A. Grounds, R. Still, and K. Takashina, *Sci Rep* **2**, 720 (2012), publisher: Nature Publishing Group.
  - [10] F. Celestini, T. Frisch, and Y. Pomeau, *Phys. Rev. Lett.* **109**, 034501 (2012), publisher: American Physical Society.
  - [11] A. Bouillant, T. Mouterde, P. Bourrianne, A. Lagarde, C. Clanet, and D. Quéré, *Nature Phys* **14**, 1188 (2018), publisher: Nature Publishing Group.
  - [12] M. A. J. v. Limbeek, M. H. K. Schaarsberg, B. Sobac, A. Rednikov, C. Sun, P. Colinet, and D. Lohse, *Journal of Fluid Mechanics* **827**, 614 (2017).
  - [13] G. Graeber, K. Regulagadda, P. Hodel, C. Küttel, D. Landolf, T. M. Schutzius, and D. Poulikakos, *Nat Commun* **12**, 1727 (2021), publisher: Nature Publishing Group.
  - [14] P. Chantelot and D. Lohse, *Phys. Rev. Lett.* **127**, 124502 (2021), publisher: American Physical Society.
  - [15] S. Shi, C. Ma, S. Hardt, and C. Lv, *Science Advances* **11**, eadt6677 (2025), publisher: American Association for the Advancement of Science.
  - [16] H. Linke, B. J. Alemán, L. D. Melling, M. J. Taormina, M. J. Francis, C. C. Dow-Hygelund, V. Narayanan, R. P. Taylor, and A. Stout, *Phys. Rev. Lett.* **96**, 154502 (2006), publisher: American Physical Society.
  - [17] X. Ma, J.-J. Liétor-Santos, and J. C. Burton, *Phys. Rev. Fluids* **2**, 031602 (2017), publisher: American Physical Society.
  - [18] T. R. Cousins, R. E. Goldstein, J. W. Jaworski, and A. I. Pesci, *Journal of Fluid Mechanics* **696**, 215 (2012).
  - [19] G. Lagubeau, M. Le Merrer, C. Clanet, and D. Quéré, *Nature Phys* **7**, 395 (2011), publisher: Nature Publishing Group.
  - [20] G. Dupeux, T. Baier, V. Bacot, S. Hardt, C. Clanet, and D. Quéré, *Physics of Fluids* **25**, 051704 (2013).
  - [21] S. Dorbolo, N. Vandewalle, and B. Darbois Texier,

- Physics of Fluids **28**, 123601 (2016).
- [22] J. C. Burton, A. L. Sharpe, R. C. A. van der Veen, A. Franco, and S. R. Nagel, Phys. Rev. Lett. **109**, 074301 (2012), publisher: American Physical Society.
  - [23] A. Bouillant, T. Mouterde, P. Bourrianne, C. Clanet, and D. Quéré, Phys. Rev. Fluids **3**, 100502 (2018), publisher: American Physical Society.
  - [24] I. U. Vakarelski, N. A. Patankar, J. O. Marston, D. Y. C. Chan, and S. T. Thoroddsen, Nature **489**, 274 (2012), publisher: Nature Publishing Group.
  - [25] S. Hidalgo-Caballero, Y. Escobar-Ortega, and F. Pacheco-Vázquez, Phys. Rev. Fluids **1**, 051902 (2016), publisher: American Physical Society.
  - [26] F. Pacheco-Vázquez, R. Ledesma-Alonso, J. Palacio-Rangel, and F. Moreau, Phys. Rev. Lett. **127**, 204501 (2021), publisher: American Physical Society.
  - [27] A. Bouillant, B. Lafoux, C. Clanet, and D. Quéré, Soft Matter **17**, 8805 (2021), publisher: Royal Society of Chemistry.
  - [28] F. Pacheco-Vázquez, M. Aguilar-González, and L. Victoria-García, Phys. Rev. Lett. **133**, 234001 (2024), publisher: American Physical Society.
  - [29] D. Paulovics, T. Frisch, C. Raufaste, and F. Celestini, Phys. Rev. Fluids **9**, L112001 (2024), publisher: American Physical Society.
  - [30] J. H. Snoeijer, P. Brunet, and J. Eggers, Phys. Rev. E **79**, 036307 (2009), publisher: American Physical Society.
  - [31] T. Baier, G. Dupeux, S. Herbert, S. Hardt, and D. Quéré, Phys. Rev. E **87**, 021001 (2013), publisher: American Physical Society.
  - [32] B. Sobac, A. Rednikov, S. Dorbolo, and P. Colinet, Phys. Rev. E **90**, 053011 (2014), publisher: American Physical Society.
  - [33] B. Sobac, A. Rednikov, and P. Colinet, Journal of Fluid Mechanics **1010**, A47 (2025).
  - [34] S. R. Waitukaitis, A. Zuiderwijk, A. Souslov, C. Coulais, and M. van Hecke, Nature Phys **13**, 1095 (2017), publisher: Nature Publishing Group.
  - [35] S. Waitukaitis, K. Harth, and M. van Hecke, Phys. Rev. Lett. **121**, 048001 (2018), publisher: American Physical Society.
  - [36] D. Bonn, M. M. Denn, L. Berthier, T. Divoux, and S. Manneville, Rev. Mod. Phys. **89**, 035005 (2017), publisher: American Physical Society.
  - [37] T. Divoux, E. Agoritsas, S. Aime, C. Barentin, J.-L. Barrat, R. Benzi, L. Berthier, D. Bi, G. Biroli, D. Bonn, P. Bourrianne, M. Bouzid, E. D. Gado, H. Delanoë-Ayari, K. Farain, S. Fielding, M. Fuchs, J. v. d. Gucht, S. Henkes, M. Jalaal, Y. M. Joshi, A. Lemaître, R. L. Leheny, S. Manneville, K. Martens, W. C. K. Poon, M. Popović, I. Procaccia, L. Ramos, J. A. Richards, S. Rogers, S. Rossi, M. Sbragaglia, G. Tarjus, F. Toschi, V. Trappe, J. Vermant, M. Wyart, F. Zamponi, and D. Zare, Soft Matter **20**, 6868 (2024), publisher: The Royal Society of Chemistry.
  - [38] J. Binysh, I. Chakraborty, M. V. Chubynsky, V. L. D. Melian, S. R. Waitukaitis, J. E. Sprittles, and A. Souslov, Phys. Rev. Lett. **131**, 168201 (2023), publisher: American Physical Society.

# Supplementary Information

## I Finite elements simulations

We use the finite element method (FEM), implemented in COMSOL MULTIPHYSICS, version 6.1, to calculate the radially dependent temperature profile of the substrate underneath the hydrogel. We perform a 2D axisymmetric simulation by placing a truncated hydrogel sphere above a sapphire surface as shown the the Fig.S1.

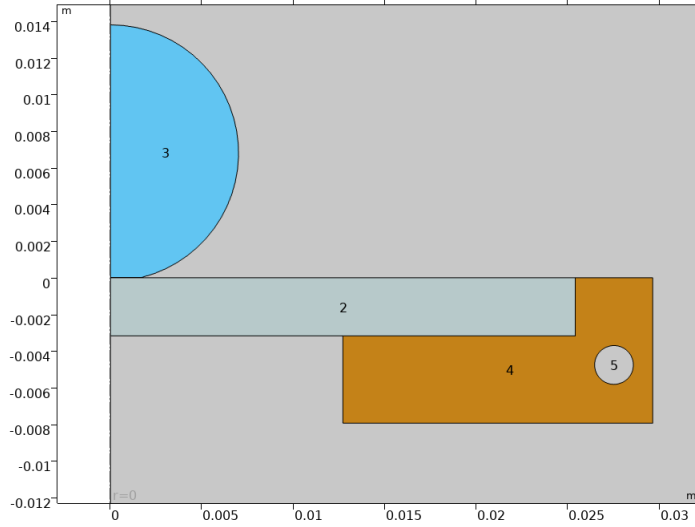


Figure 1: Geometry used in the finite element method (FEM) simulations. We performed 2D axisymmetric simulations using COMSOL MULTIPHYSICS, where a truncated hydrogel sphere is placed above a sapphire substrate.

The gap height corresponds to the truncation radius and follows the relation:

$$h_0(t) = \left( \frac{3\pi\eta\kappa\Delta T}{2\rho L} \right)^{\frac{1}{4}} \frac{R(t)}{(mg)^{1/4}}. \quad (1)$$

This relation is valid for both liquid droplets and hydrogels. The sapphire substrate is in contact with a copper heater. We solve the heat transfer equation for the geometry described above, applying the following boundary conditions: internal boundaries in contact with the heater are set to 300°C, while the boundaries of the hydrogel are maintained at 100°C. The surroundings of both the hydrogel and the heater are modeled as air, with thermally insulating (adiabatic) boundary conditions.

The initial conditions assume the hydrogel is at  $100^{\circ}\text{C}$ , and both the sapphire and heater are at  $300^{\circ}\text{C}$ . A physics-controlled mesh with an extremely fine element size is used to ensure numerical accuracy.

We perform a stationary study for different truncation radii, yielding the temperature profiles used in the local mass loss calculations described in the main text (Fig.S2).

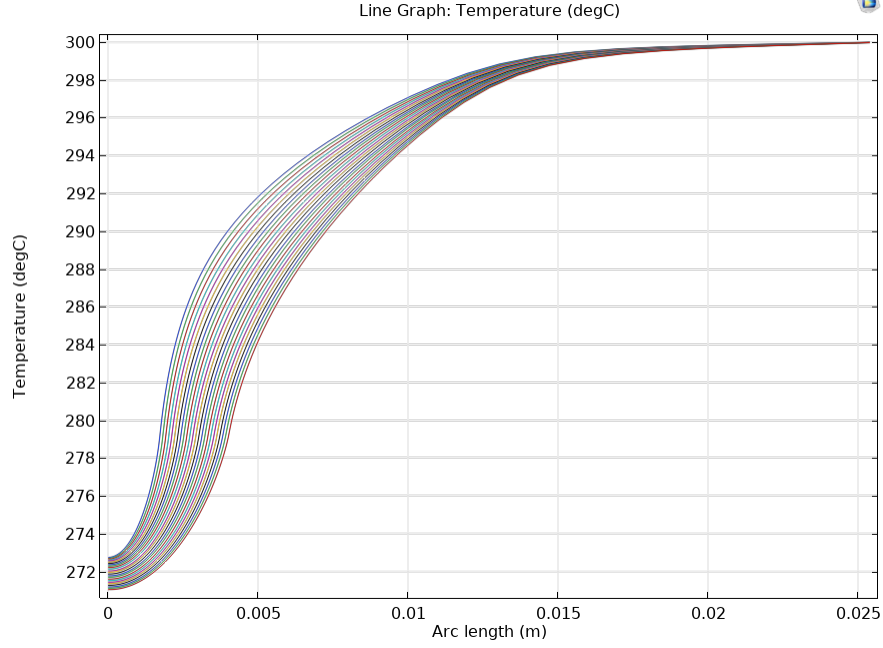


Figure 2: Steady-state temperature profiles at the top surface of sapphire windows for varying truncated radii.

## II Reaching of our optical setup

We measured the lateral diameter of the truncated hydrogel in two different ways: (1) from the side using a camera, and (2) by analyzing the diameter of the interference pattern. The side-view image of the hydrogel was fitted using a piecewise function, where the curved region was approximated with a parabola and the truncated section with a straight line. The distance between the intersections of the two parabolic fits was taken as the lateral diameter in the side view. In the case of the interference pattern, the diameter was measured directly from the pattern. Fig.S3 shows that the two measurements closely match, providing evidence that we can reliably access all the optical features beneath the hydrogel.

## III Contribution of Heat and Concentration Fluxes to Height Variation

The mass loss process is a key component that defines the final shape of the underbelly hydrogel. In this system's geometry, vaporization can originate mainly from two sources:



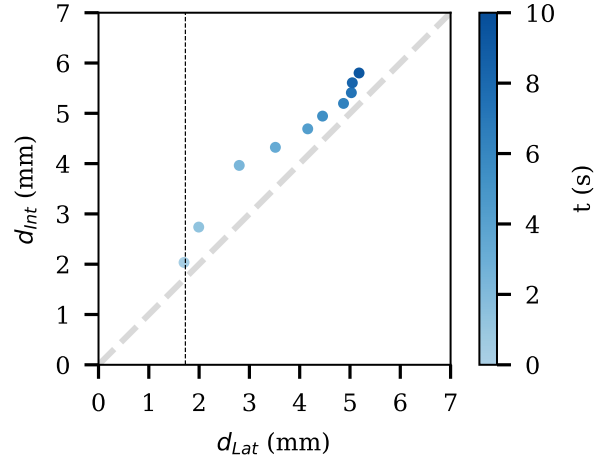


Figure 3: Lateral diameter measured from the side-view camera image versus the diameter obtained from the interference pattern. The strong agreement between the two methods indicates reliable access to the optical features beneath the hydrogel

the heat flux and the water concentration gradient in the vapor layer.

For the heat flux ( $\vec{J}_q$ ), heat conduction is dominant. We use Fourier's Law (Equation 2) to calculate the local variation in height as a consequence of the temperature gradient  $\nabla T$ , where  $\kappa$  is the thermal conductivity:

$$\vec{J}_q = -\kappa \nabla T \quad (2)$$

Assuming temperature changes only along the  $z$ -axis for local vaporization and adapting to polar coordinates, we derive Equation 3, where  $L$  is the latent heat of vaporization:

$$\delta M = -\frac{\kappa}{L} \frac{\partial T}{\partial z} 2\pi r dr \delta t \quad (3)$$

Here,  $\delta M$  is the mass variation over the time interval  $\delta t$  along the truncated region of the hydrogel. Using the definition of density  $\rho$ , we relate mass variation  $\delta M$  to the local height variation  $\delta h$  (Equation 4):

$$\delta M = \rho dV = \rho 2\pi r dr \delta h \quad (4)$$

Combining Equations 3 and 4, and applying the thin-layer approximation, we obtain the height variation as a function of time (Equation 5). Here,  $h(r)$  is the absolute height at a radial position  $r$ ,  $T(r)$  is the radial temperature profile, and  $T_H$  is the hydrogel temperature:

$$\delta h = -\frac{\kappa}{L\rho} \frac{T(r) - T_H}{h(r)} \delta t \quad (5)$$

For the case of vapor concentration in the vapor layer, we use Fick's Law (Equation 6) to relate the concentration flux ( $\vec{J}_\phi$ ) with the concentration gradient ( $\nabla \phi$ ), where  $D$  is the

diffusion coefficient:

$$\vec{J}_\phi = -D\nabla\phi \quad (6)$$

By applying the definition of concentration flux in polar coordinates, and using the relation between mass and concentration via molar mass ( $M$ ), together with Equation 4, we derive the height variation due to concentration gradient (Equation 7):

$$\delta h = -\frac{DM}{\rho}\nabla\phi\delta t \quad (7)$$

From the ideal gas law, we relate concentration  $\phi$  to pressure  $P$ , where  $R$  is the ideal gas constant and  $T$  is the temperature:

$$\phi = \frac{P}{RT} \quad (8)$$

From lubrication theory, the pressure profile underneath the hydrogel is given by Equation 9, where  $\mu$  is the viscosity,  $h_0$  is the absolute current height,  $P_{\text{atm}}$  is atmospheric pressure,  $r_{\text{trun}}$  is the truncated radius, and  $r$  is the radial position:

$$P(r) = \frac{3\mu W_0}{h_0^3}(r^2 - r_{\text{trun}}^2) + P_{\text{atm}} \quad (9)$$

$W_0$  is defined as:

$$W_0 = \frac{\kappa(T(r) - T_H)}{\rho L h_0} \quad (10)$$

Combining Equations 7, 8, 9, and 10, we obtain the height variation due to concentration flux as:

$$\delta h = -\frac{6DM\mu\kappa}{\rho^2 R T_H L h_0^4}(T(r) - T_H)r\delta t \quad (11)$$

Following the computational steps described in the main text, we calculate the height variation over discrete time steps. Figure S4 shows the results for the initial stages, where it is evident that the heat flux has a more significant impact on height variation compared to the concentration flux.

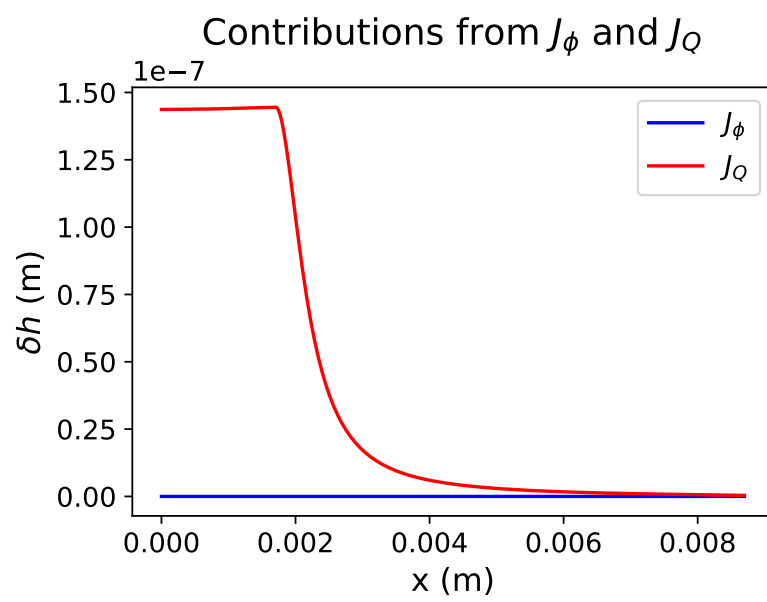


Figure 4: Caption